Supporting Information for

"Lower-mantle substructure embedded in the Farallon Plate: The Hess Conjugate"

Justin Yen-Ting Ko[1*], Don Helmberger[1], Huilin Wang[1], and Zhongwen Zhan[1]

[1]Seismological Laboratory, Division of Geological and Planetary Sciences, California Institute of Technology, 1200 East California Blvd, Pasadena, CA 91125, USA.

Contents of this file

1. Modeling waveform complexity

Global seismic tomography is making major gains with comparisons of 1D and 3D synthetics online for many significant earthquakes (http://global.shakemovie.princeton.edu), see Tromp et al. [2010]. However, typical 1-D synthetics agree better with the 3D travel-time predictions than either fit the observed waveforms, even at 20s or longer [Li et al., 2014]. Thus, 2D models have been developed to improve images which can then be checked against SEM results as in Chen et al. [2007] or in using 3D adjoint method [Tromp et al., 2008]. This is especially true at shorter periods since computational cost scales as the 4^{th} power of frequency in SEM. Note that the waveform complexity we are attempting to model becomes particularly observable at the shorter periods as displayed in Fig. 4.

Higher order finite difference greatly reduces numerical dispersion but can develop problems at the free surface, i.e. sharp velocity discontinuities [*LeVander,* 1988]. Thus, the advanced 2D code used here has been extensively tested against the various methods in earlier versions, Vidale et al. [1985], both against analytical solutions (see Figs. 6 and 7 of Helmberger et al. [1985]) and hybrid methods as discussed in Li et al. [2014b] for frequencies up to 3 Hz, see their Figs. 10 and 14. In short, this new code becomes particularly useful in modeling waveform complexity.

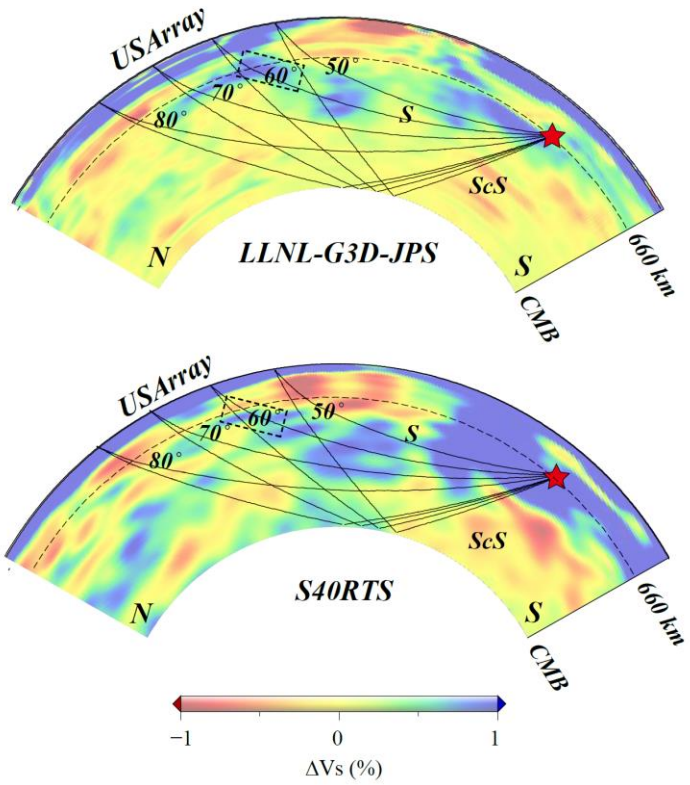

Figure S1. 2-D cross-sections of shear-wave tomographic models with seismic ray paths of S and ScS waves at different epicentral distances obtained for the LLNL [Simmons et al., 2015] and S40RTS [Ritsema et al., 2010] models. The dashed box approximately delineates the south-dipping fast anomaly around 60° of S wave in each tomographic model.

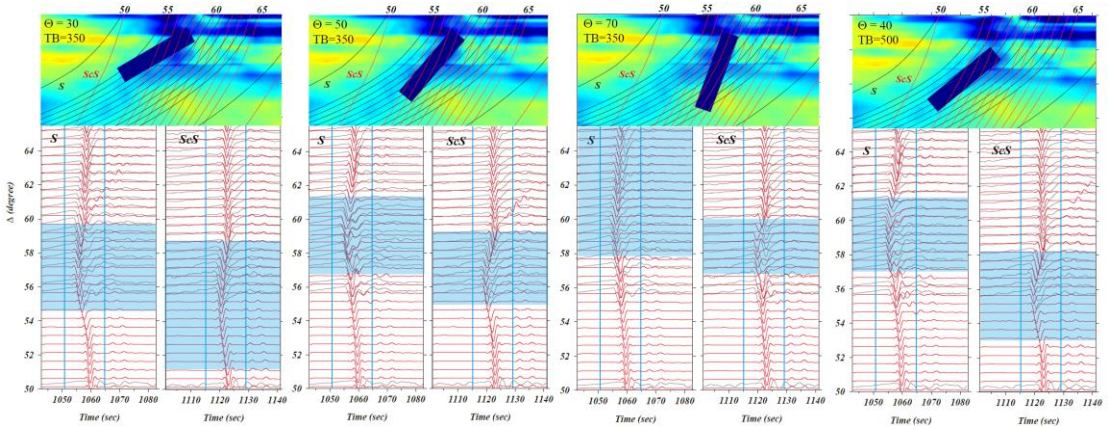

Figure S2. The sensitivity tests for the slab dip angle and top boundary. The grey and red lines represent data and synthetics, respectively. The blue zones indicate the anomalous area caused by the slab-like structure. Note that the significant shift of the anomalous area between S and ScS. The strong waveform distortions are observed while the structural dip angle is parallel to the ray paths, i.e. 50° for S and 70° for ScS. Note that the change in top boundary (TB) with a slight rotation of structural dip angle can return a similar fit to the data, if compared to the first and final models. These four trail models were denoted by yellow circles in Fig. 3c.

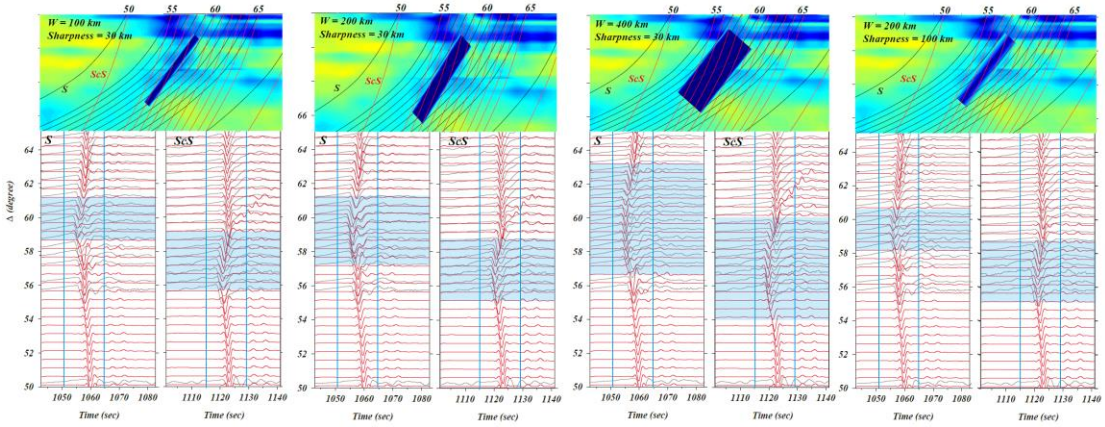

Figure S3. The sensitivity tests for the slab width and sharpness. The grey and red lines represent data and synthetics, respectively. The blue zones indicate the anomalous area caused by the slab. The slab width and sharpness directly influence the effective area of waveform distortions caused by the anomaly. The thicker the slab the larger the anomalous area is observed. Given a triangle velocity gradient across the slab-like structure will narrow down the waveform distortion region compared to the perfectly sharp edges. These four trail models were denoted by yellow circles in Figure 3d.

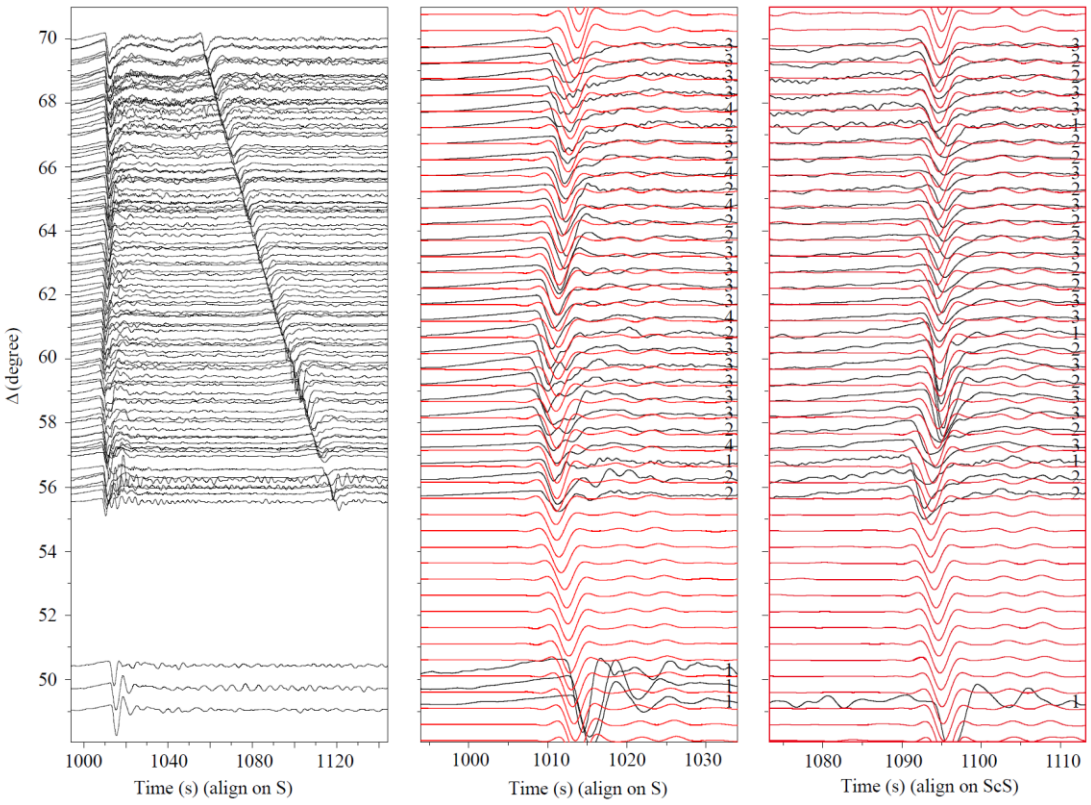

Figure S4. The waveform comparison between data (black) and synthetics (red) computed by FD using the LLNL model.

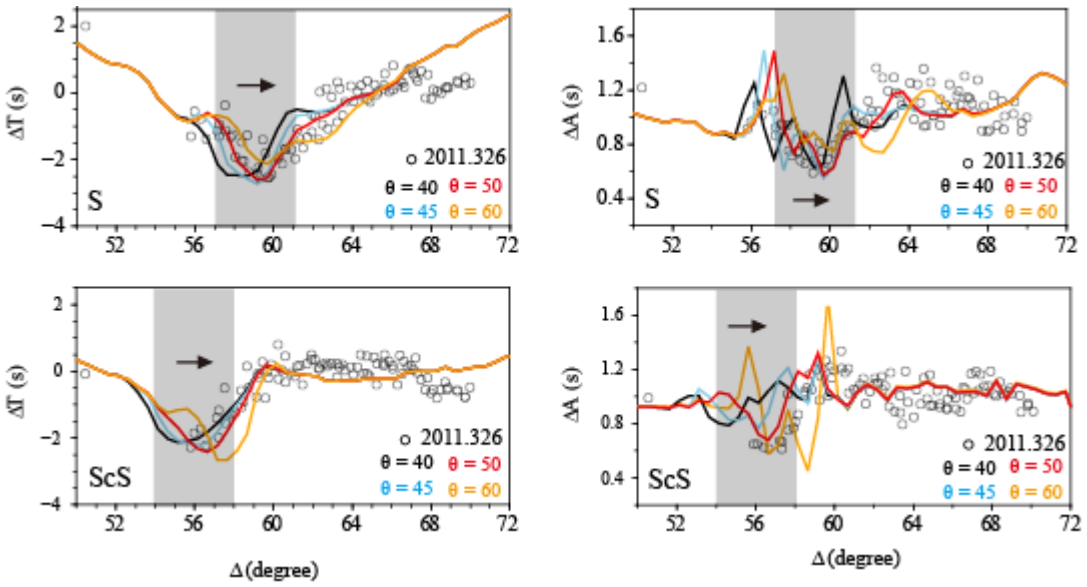

Figure S5. The model sensitivity to the structural dip angle. The black circle displays the data. The shaded areas indicate the observed waveform distortions displayed in Figure 2b. The synthetic waveforms and corresponding travel time and amplitude fluctuations compared to PREM are calculated by the FD in four trial models with θ ranging from 40° to 60° with different colors labeled on the bottom-right corner.

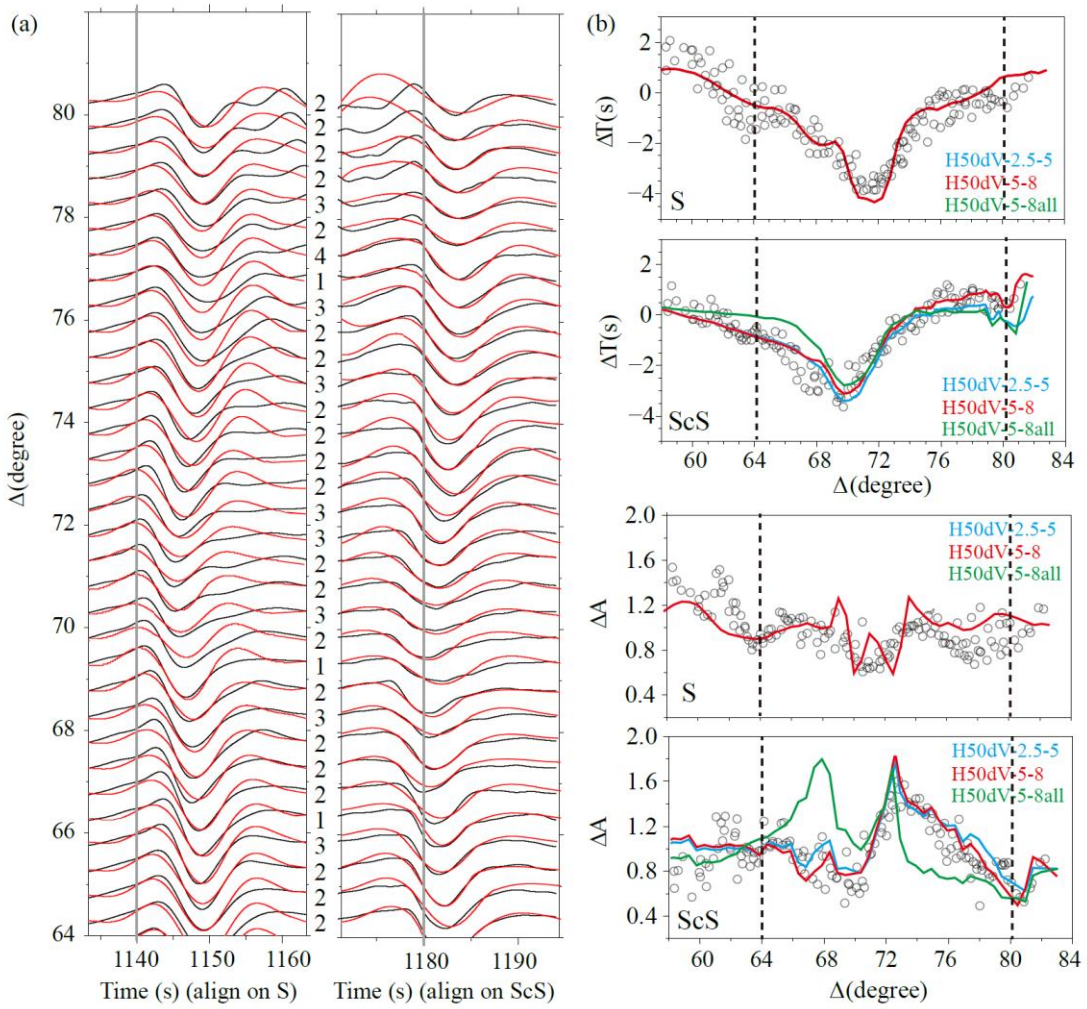

Figure S6. Comparison of the data and synthetics for the event 2012.149. (a) The black lines are observed waveforms and the red lines indicate the synthetic waveforms obtained from our preferred model. (b) Contains the comparison of relative travel times (PREM) and amplitudes for three models. Here, the PLVS has a height of 50k m and has two possible reduced velocities, -2.5% (top) to -5% at bottom (blue) or -5% to -8% (red). The third model has the width of the PLVS extended for all events (green).

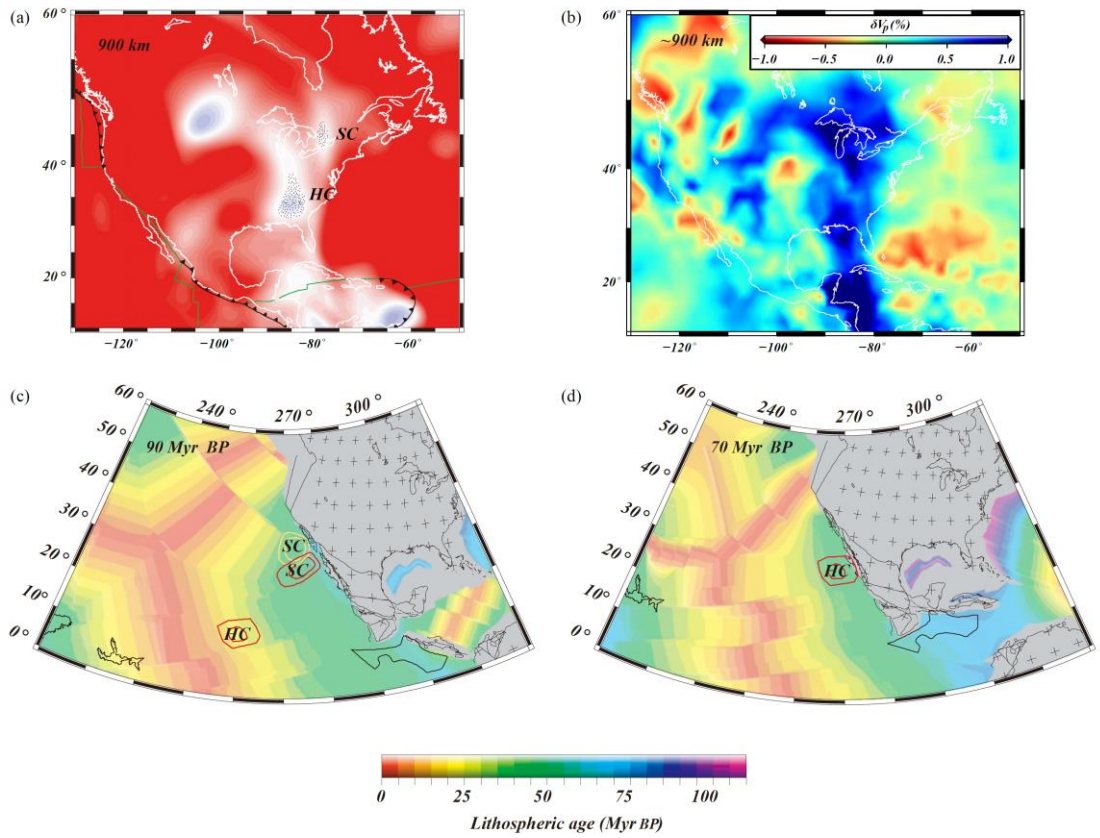

Figure S7. The history of the Shatsky conjugate (SC) and the Hess conjugate (HC) and the linkage to the tomographic images. (a) The estimated present location of the subducted HC (The black dots). (b) Map view of the LLNL model at ~900 km depth displaying the tomography image of the Farallon slab in the mid mantle and geological features related to the flat subduction. The fast anomaly beneath the Caribbean is expected from normal slab fall. The middle zone at the northern edge of the Gulf of Mexico appears to be associated with the HC while the northern patch appears to be dipping to the North-East, perhaps the SC. (c) The locations of the SC and HC in the Late Cretaceous predicted by plate reconstruction. The yellow and red positions indicate the differences between methodologies. Modified from Liu et al. (2010).

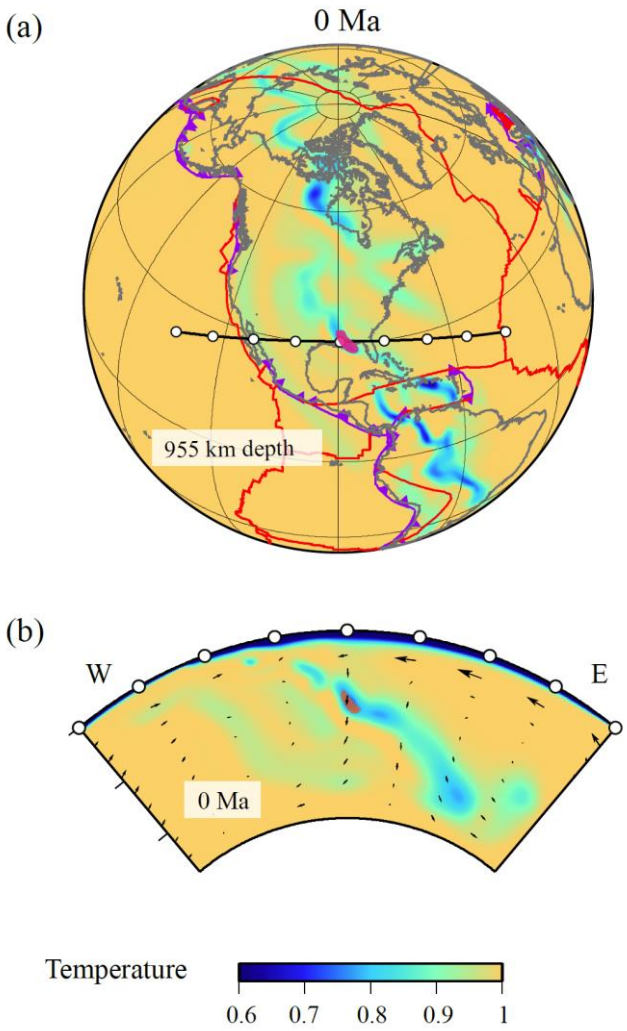

Figure S8. Dynamic topography evolution above the Hess conjugate in the context of hemispheric mantle temperature anomalies. (a) Modeled non-dimensional temperature anomaly at the given depths and ages. The red highlighted region around the GOM denotes the location of the Hess conjugate. (b) Cross sections of thermal structures (orientation of profile shown in Fig. S8a). Modified from Wang, H., Gurnis, M., and Skogseid J., 2017, Rapid Cenozoic subsidence in the Gulf of Mexico resulting from the Hess Rise conjugate subduction, manuscript submitted for publication.

	Time	Longitude	Latitude	Depth	Mw
2012.05.28 (149)	**05:07:23.45**	**-63.094**	**-28.043**	**586.9**	**6.7**
2011.11.22 (326)	**18:48:16.29**	**-65.163**	**-15.308**	**560.3**	**6.6**
2012.11.22 (327)	**13:07:10.42**	**-63.571**	**-22.742**	**516.6**	**5.9**
2013.02.22 (053)	**12:01:59.20**	**-63.195**	**-27.993**	**585.8**	**6.1**
2012.06.02 (154)	**07:52:53.99**	**-63.555**	**-22.059**	**527.0**	**5.9**

Table S1. Five events contributed to the minimization of the cost function used in the inversion. The event origin time, location and magnitude are based on IRIS dataset.

Parameters	Minimum	Maximum	Interval	Optimal
Dip	30°	70°	10°	40° to 50°
Top boundary	150 km	700 km	50 km	300 or 500 km
Width	100 km	400 km	50 km	200 km
Sharpness	0 km	100 km	10 km	50 km
Length	500 km	1500 km	250 km	1000 km
Velocity	1%	4%	0.5%	2.5%

Table S2. The range of the model variables used in the grid search.